Chapter 2

Optimizing the Detector Geometry of In-Beam PET

2.1 Motivation

The first attempts in operating an in-beam positron tomograph at the Lawrence Berkeley National Laboratory (LBNL) had to be abandoned due to detector activation arising most probably from passive beam shaping contaminations [Lla88]. To avoid this with good security margins, and because of the patient positioning restrictions imposed by the fixed, horizontal beam line at the GSI pilot project, together with the fact that first-planned treatments consisted of small-sized tumors only, a dual-head positron camera was installed (Fig 1.18). This was done after careful research that garanteed the imaging capabilities of the selected tomograph [Paw96], including a synchronization of in-beam PET data with the macrostructured particle extraction delivered by the synchrotron (section 1.4.2). To cope with such limited-angle tomograph a dedicated, attenuation correcting, maximum likelihood expectation maximization algorithm MLEM [Lau99] with a correction for single-Compton events occurring in the object [Pön03a, Pön03b] was developed. All these developments contributed to the success of in-beam PET for monitoring, in clinical routine, the carbon ion irradiation at the GSI pilot project [Eng04b].

With the clinical results achieved prompting the construction of a dedicated hospital facility where in-beam PET is expected to monitor more delicate therapeutic situations, optimizing the detector geometry after having learned the unavoidable limitations of the presently installed tomograph becomes a priority. The first challenge was to develop a simulation and a reconstruction routine capable of handling a higher number of coincidence channels than the reconstruction installed at GSI. There, each head of the tomograph contains 2 048 detector elements resulting in about 4.2 million coincidence channels. If the ECAT® EXACT™ HR$^+$ tomograph (CTI PET Systems Inc.) is considered, containing 32 complete detector rings, the number of single detectors raises to 18 432. Since in-beam PET is characterized by data-sets of low statistics, rebinning the 3D collected data into 2D sets disturbs the spatial information of the few lines-of-response (LOR) existing, which vetoes the application of already existing rebinning algorithms. Because of the enormous amount of crystal combinations possibilities, close to 170 million, dynamic memory allocation is necessary together with a factorization scheme that allows the reconstruction to handle only non-empty coincidence channels [Cre02]. Therefore, a set of routines was developed in order to simulate and reconstruct in real 3D the mentioned full-ring tomograph. Furthermore, the routine sets are able to handle dual-head tomographs with different opening angles so that, whatever tomograph geometry is found to be optimum, reconstruction restrictions will not pose a problem to next-generation, in-beam PET scanners at future heavy ion clinics.

2.2 Reconstruction of PET List Mode Data

Image reconstruction algorithms are usually divided into two categories: analytic and iterative methods. Analytic methods assume that the measured data approximate line integrals through the radioisotope distribution and use the widely accepted filtered backprojection (FBP) technique [Bro76]. Although this is not an exact method (mathematically an infinite number of projections is assumed, when only a finite number of projections are acquired), the results are precise enough for most medical applications. A major advantage is the speed of reconstruction achieved: current scanners process, with this method, a stack of 2D slices forming a 3D image in only a few minutes. The major disadvantage, besides noise and poorer spatial resolution when compared to iterative methods, lies on the fact that this method requires the detector response to be space-invariant. This requirement is only satisfied by positron cameras that cover completely their field of view (FOV), i.e. ring-shaped or rotating dual-head cameras. Iterative methods, despite of their large amount of computing time and power required, yield better images for they are based on exact mathematical models. In fact, in high resolution PET and when areas with low tracer uptake are in close vicinity to hot spots, e.g. in liver tumors, iterative reconstruction methods are of special interest, as FBP frequently yields non-conclusive results in these special cases. A further advantage of algebraic techniques is that the physics involved with imaging, including attenuation and scatter, can be included into the reconstruction algorithm. For the present study case, analytic methods were ruled out to start with as the space-invariant requirement is not fulfilled by dual, fixed-head PET camera geometries. Thus, the maximum likelihood expectation maximization algorithm, already applied to the BASTEI camera [Lau99] and described by Shepp and Vardi in great physical and mathematical detail [She82], was also applied to detector geometries similar to that of the ECAT EXACT HR$^+$ scanner from CTI PET Systems, Inc.

2.2.1 The maximum likelihood expectation maximization algorithm

The maximum likelihood expectation maximization method describes the process of imaging as

$$y_j = \sum_i a_{ij} x_i, \tag{2.1}$$

with x_i the activity of the i^{th} voxel contributing with weight a_{ij} to the j^{th} coincidence channel. However, the inversion of matrix $\boldsymbol{A} = \{a_{ij}\}$ in Eq. 2.1 which would lead to a direct solution for $\mathbf{x}$ is impossible since the problem is ill-posed for several reasons: (1) the matrix elements a_{ij} are not exactly known, since they depend on x_i (due to Compton scattering), (2) there may be not enough projections acquired to provide a sufficient number of equations and, even if the number of equations were sufficient, (3) the statistical nature of the radioactive decay and its detection would introduce ambiguities into the system of equations. Therefore, an iterative procedure must be applied. This procedure can be deduced by considering that the probability of observing a measured coincidence channel distribution $\boldsymbol{y} = \boldsymbol{y}_{meas}$, given a hypothetical activity distribution $\boldsymbol{x}_{hyp}$, can be maximized by applying the likelihood function to these variables. The probability of success, i.e. detecting the activity of one voxel x_i in a particular coincidence channel y_j, is much smaller than the total number of possibilities, which makes the detection process Poisson-like. Because a pair of photons interacting in a pair of detectors will not be detected in any other channel (neglecting Compton effect in the crystals), the variables are then Poissonian and independent. This allows the Poisson distribution to be applied, being that $\mathrm{P}(\boldsymbol{y}_{meas} \,|\, \boldsymbol{x}_{hyp})$ is the probability to be maximized via the likelihood function. Manipulation of that function proves that the likelihood is concave (convergence

exists) and by appling a maximization expectation algorithm Eq. 2.2 can be obtained:

$$x_i^{(n)} = x_i^{(n-1)} \sum_j a_{ij} \frac{y_j}{\sum_k a_{kj} x_k^{(n-1)}}. \tag{2.2}$$

Eq. 2.2 represents the maximum likelihood expectation maximization (MLEM) algorithm, with $n = 1 \ldots$ iteration number, $i = 1 \ldots$ number of voxels in image, $k = 1 \ldots$ number of voxels in image, and $j = 1 \ldots$ number of coincidence channels. The vector $\boldsymbol{x}^{(0)}$ is the starting homogeneous image. The matrix elements a_{ij} are difficult to compute and to store due the enormous size of $\boldsymbol{A}$[1], so they are calculated in each reconstruction step by using an approximation.

2.2.2 Routine stability and optimization

The algorithm described in the previous section was applied to the ECAT EXACT HR$^+$ scanner detector geometry. A simulation was developed that creates list mode data sets that can be read by this routine. The simulation can consider full ring detector arrangements, as well as any camera with two gaps (Fig. 2.1) with sizes given by an integer number of missing detector blocks. Although the size of the simulated detector pixels can be changed by the user with the simulation and reconstruction codes proceeding automatically, all results presented here refer to detector pixels with 5 mm in the axial direction (Z_{PET}) and approximately 4.5 mm in the transaxial direction. The radial depth of the scintillator material was changed between 0, 20 and 30 mm, corresponding to a simulation of the geometrical acceptance of the tomograph only (0 mm) as well as to the efficiency of coincidence detection, as detailed in the next sections.

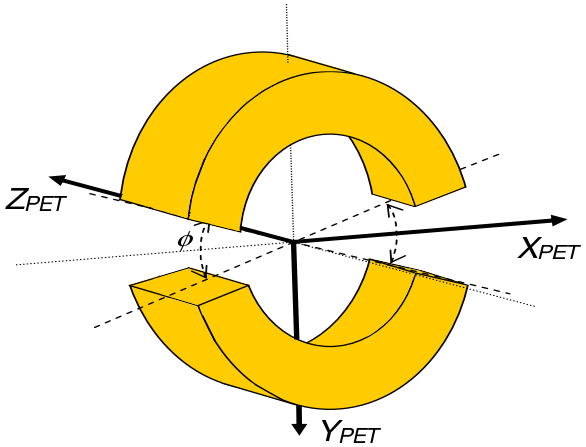

Figure 2.1: Scheme of the dual-head positron camera studied. The gap between the two detector heads defines the angle ϕ at the isocenter, with $\phi = 0\,^\circ$ representing a closed ring camera.

Reconstruction artifacts from discrete sampling and its correction

Although the annihilated photons are emitted isotropically, their sampling is discrete with a step imposed by the detector size. The on-line calculation of the a_{ij} coefficients considers, for each coincidence channel with a non-zero value, the line that connects the two corresponding detectors. This line approximation, if taken singularly, will introduce artifacts in the image, leading to the appearence of false grains in image points corresponding to crossings of detectors centers. Due to the sensitivity of the MLEM algorithm to high spatial frequencies, these points will be maximized and lead to false, unstable images if no further action is taken. Fig. 2.2 depicts this problem in the left and middle images, and its solution in the right image.

[1] The dimensions of matrix $\boldsymbol{A}$ is on the order of 65000×65000 for a single plane of a typical scanner.

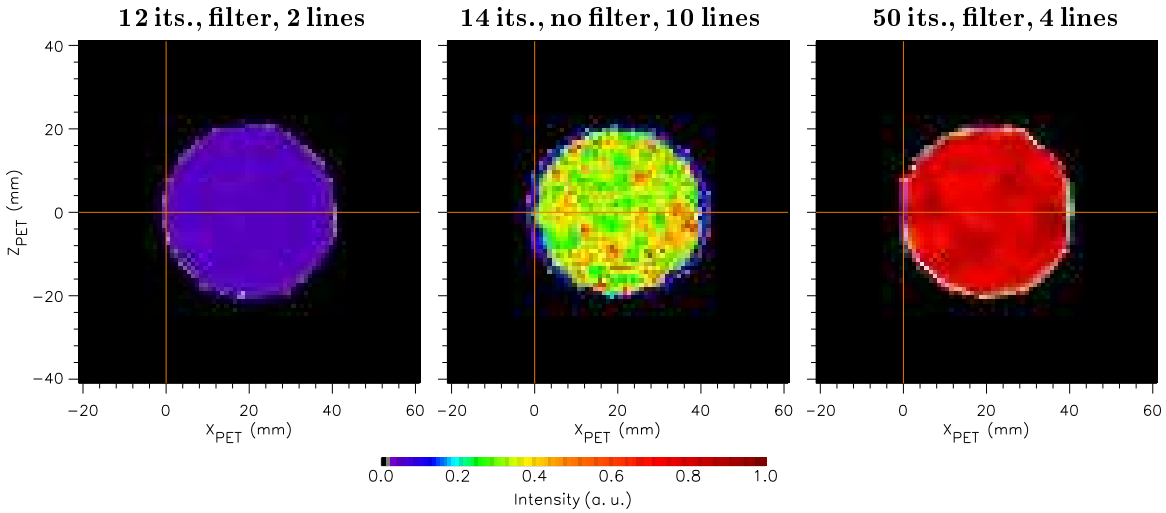

Figure 2.2: Removal of the granularity effect due to detector size. The images show reconstructed datasets from a simulated sphere of activity with 20 mm radius and center shifted by 20 mm along X_{PET}. A closed ring camera was considered. The left image was obtained with a spatial filter applied between each iteration and with 2 lines filling each LOR. In the middle image no filter was applied and 10 lines filled each LOR. Finally, routine stability was achieved when the spatial filter is applied even with 4 lines only filling each LOR. All images were solid angle corrected.

A common approach in iterative algorithms where the matrix **A** is not available is the simulation of several lines within each LOR connecting two detectors. This reduces the algorithm time performance but brings stable images if the number of lines is high enough. The number of simulated lines per LOR can be reduced by applying a spatial filter (median of each voxel with its 26 neighbours) to the object image between each iteration, thus increasing the performance of the algorithm in terms of time with no compromise in image stability and quality (Fig. 2.2).

2.3 Detection Efficiency with Several Detector Arrangements

The arrangement of the detectors in a tomograph and its intrinsic geometry, e.g. scintillator depth, result in different coincidence detection efficiencies that need to be known before a tomograph is chosen for the Heidelberg heavy ion clinics and, therefore, are presented in section 2.3.1. In addition, this knowledge is necessary in order to correct, in each iteration step of the reconstruction algorithm, each image voxel with its corresponding solid angle value, given in section 2.3.2. Furthermore, the effect of low-statistics images in regions with very small solid angle values is also presented.

2.3.1 Quantification of detection efficiencies

Fig. 2.3 shows the dependence of the coincidence detection efficiency of several tomographs with a sphere of activity with radius ranging from 1 to 200 mm centered in their FOV. The top graph depicts the geometrical coincidence detection efficiency. By allowing the annihilation photons to penetrate into the scintillator material the coincidence detection efficiency was obtained for tomographs with crystals of lutetium oxyortholsilicate (LSO) with a radial length of 30 mm (middle graph) and 20 mm (bottom graph). Besides taking into account the different tomograph opening angles ϕ (cf. Fig. 2.1), each graph plots two sets of curves with one corresponding to a tomograph with the dimensions of a tyical PET scanner, with an axial FOV of 16 cm and a radius of approximately 41 cm, whereas the second set of curves in each

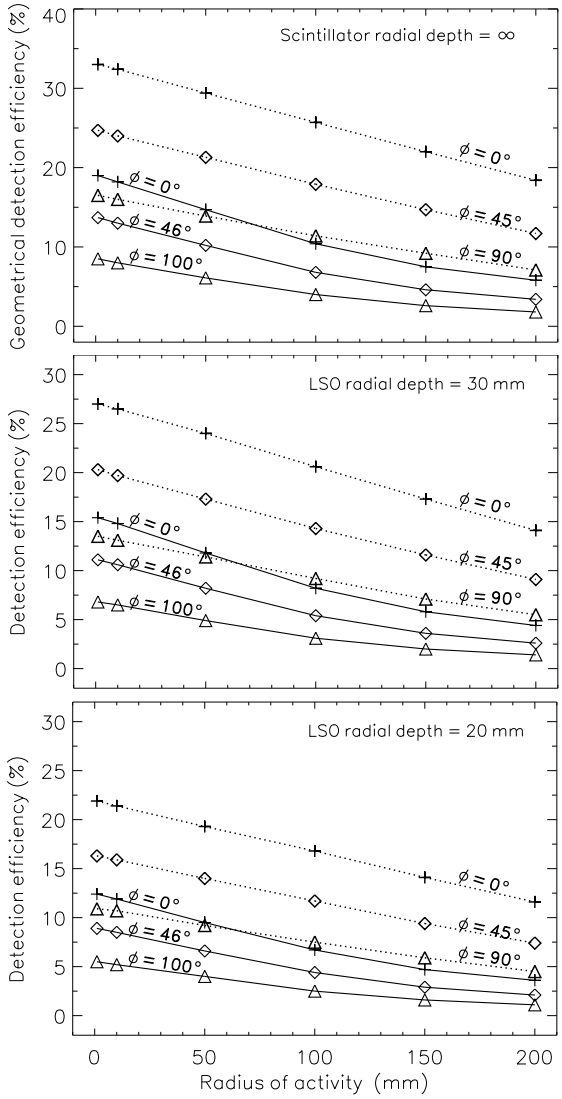

Figure 2.3: Coincidence detection efficiencies for several detector arrangements with different scintillator thicknesses and with a sphere of activity located at the isocenter. The dotted lines denote a larger tomograph with 45.8 cm inner radius and 32 cm axial length versus the 41.2 cm and 16 cm considered with the solid lines, respectively.

graph regards a possible scanner configuration better suited for in-beam PET, with doubled axial FOV and a radius of approximately 46 cm and, consequently, higher coincidence detection efficiency.

2.3.2 Geometrical solid angle

In order to be able to study the performance of several tomographs, each with different opening angles ϕ, the knowledge of their coincidence detection efficiency is necessary. Fig. 2.4 plots the solid angle distribution, i.e. the geometrical coincidence detection efficiency without taking into account the penetration of the photons in the detectors, for several tomographs: a closed-ring ($\phi = 0\,^\circ$), a dual-head, small-gaps ($\phi = 46\,^\circ$) and a dual-head, wide-gaps ($\phi = 100\,^\circ$) tomograph with dimensions approximately equal to the ECAT EXACT HR$^+$ scanner, i.e. 16 cm axial FOV and 41 cm radius. All reconstructed images shown in the present chapter were weighted between each iteration step with the corresponding solid angle distribution shown in Fig. 2.4.

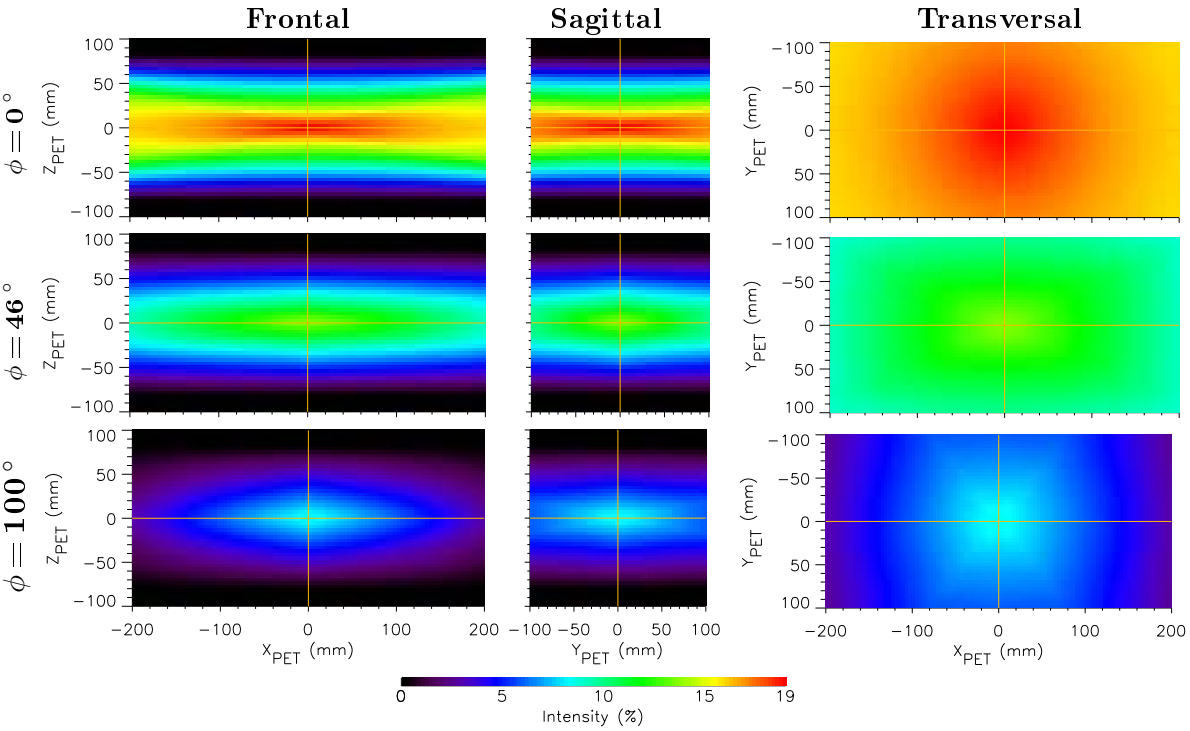

Figure 2.4: Geometrical solid angle distributions in a closed ring ($\phi = 0°$), a dual-head, small-gaps ($\phi = 46°$) and a dual-head, wide-gaps ($\phi = 100°$) tomograph.

As presented in Fig. 2.5, a smooth coincidence detection efficiency extending through the complete image space sampled is highly desirable in order to equally correct noisy images. Fig. 2.5 shows that equal noise oscillations sampled in a given signal are under- and over-ampliflied when a correction with a low coincidence detection efficiency in respect to the central, maximum value, has to be applied. This behaviour is observed in section 2.6 where its influence on simulated, real-treatment images is shown: a false, high-intensity activity arises in the beam entrance channel for images sampled with tomographs with higher coincidence detection efficiency gradients.

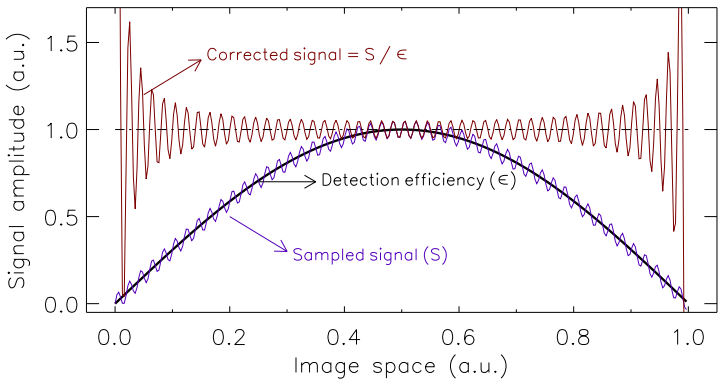

Figure 2.5: Importance of a smooth detection efficiency in noisy samples. An under- and over-amplification effect arising in noisy samples corrected with a too low detection efficiency value is shown. The average of the corrected signal is unity, as expected. But the maximum likelihood expectation maximization algorithm, being very sensitive to noise, amplifies the false noise peaks.

2.4 Degradation of Spatial Resolution with Dual-Head Scanners

Fig. 2.6 compares the spatial resolution obtained with a simulated closed ring detector geometry ($\phi = 0°$) to that obtained with a dual-head tomograph with $\phi = 100°$. Several point sources were simulated at different locations inside the FOV of tomographs with 20 mm radial depth of scintillator. The Fig. shows a 2D image and the corresponding line profile for one such point source reconstructed after 50 iterations. It can be seen that an image spread appears along the axis with missing detectors (Y_{PET}) for the dual-head geometry, which translates into a lower spatial resolution obtained along this axis. This degradation is quantified in Table 2.1 for the three axes of the tomographs at several point source locations. The values in the table included from the BASTEI tomograph were measured with ^{22}Na sources [Lau99] and cannot be directly compared with the simulated values due to several reasons: (1) the simulation does not include Compton scattering neither in the object nor in the detectors and contains singular point sources whereas the measured values contain both physical processes mentioned in addition to the intrinsic volume of the source, and (2) the values measured with BASTEI suffer from an increased spatial resolution degradation [Mos93] arising from the light sharing readout implemented at the detector level [Mos94], i.e. four photomultiplier tubes (PMT) read the 8×8 pixels of each scintillator block in modified Anger readout [Ang58].

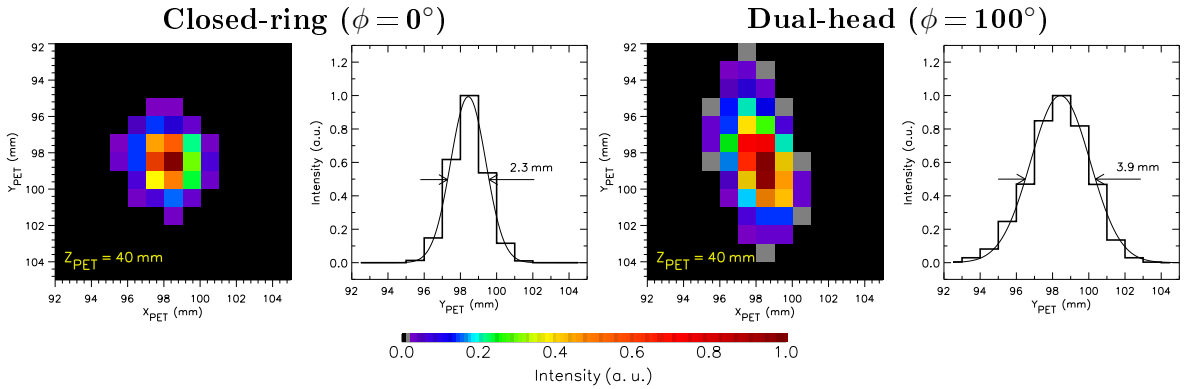

Figure 2.6: Degradation of spatial resolution from a closed ring to a dual-head tomograph.

Table 2.1: Degradation of spatial resolution from a closed ring to a dual-head tomograph.

Point source location			Closed ring			Dual-head $\phi = 100°$			BASTEI		
X_{PET}	Y_{PET}	Z_{PET}	FWHM (mm)			FWHM (mm)			FWHM (mm)		
(cm)	(cm)	(cm)	X	Y	Z	X	Y	Z	X	Y	Z
0	0	0	1.8	1.9	1.9	1.8	2.3	1.8	5	7.5	5
10	0	4	1.9	2.0	1.8	2.0	3.1	2.0	5	11	5
10	5	4	2.0	2.0	1.9	2.0	3.6	1.8	5	13	5
10	10	4	2.1	2.3	1.8	2.2	3.9	1.8	5	22.5	5

But the approximately twofold degradation of the spatial resolution in the axis with missing detectors, observed with isolated point sources, is not the main disadvantage of fixed, dual-head tomographs. The reduction of signal intensity due to this spatial spread, not shown in Fig. 2.6, represents a more important artifact to be be minimized (sections 2.5 and 2.6).

2.5 Imaging with Dual-Head Tomographs

Rare but possible patient anatomical modifications during the course of the fractionated irradiation at the GSI heavy ion therapy unit do not include only the example shown in section 1.4.2,

where in-beam PET detected a non-critical reduction of the tumor volume (Fig. 1.21). In head and neck irradiation, the filling of one or more of the sinus cavities with mucus or due to an inflammation of the surrounding tissue may also be detected by in-beam PET: when the beam crosses this filled cavity it generates there an unexpected excess of β^+ activity due to the non-empty traversed path. When such alterations of the tissue density occur the main task of in-beam PET is to detect whether a possible reduction of the beam range occurs with, consequently, an under-dosage of tumor tissue downbeam. Although occurring seldom, clinical in-beam PET allows an alert to be made to the radiotherapist in such situations. Typically, an anti-mucus drug administered to the patient is enough to solve the problem. More delicate and very rare situations may require a new CT of the patient and eventually the calculation

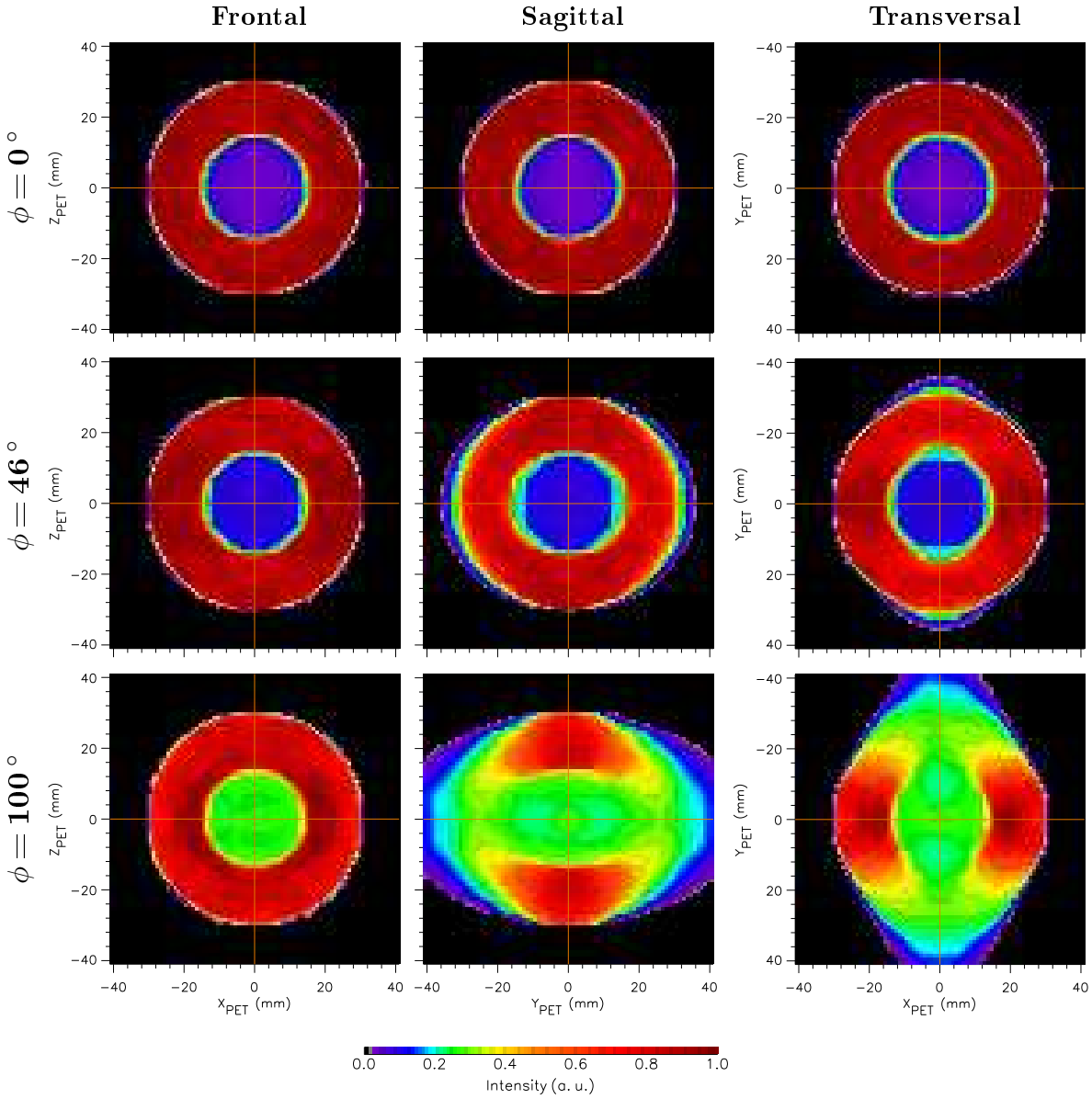

Figure 2.7: Reconstruction of a hollow sphere homogeneously filled with activity (100 million annihilations). The sphere was positioned at the isocenter of three different tomographs. The closed-ring detector configuration registered 16 million events, whereas the dual-head geometries detected 11 million ($\phi = 46\,°$) and 6 million ($\phi = 100\,°$) events.

of a new irradiation plan. Therefore, it is extremelly important that the in-beam PET images preserve the maximum information when the annihilation activity surrounds empty activity regions (air-filled cavities). In order to approximate such a situation and study the effect of the camera geometry onto in-beam PET images, the detection of the activity from a hollow sphere was simulated with three different positron cameras.

2.5.1 Precise activity volume: hollow sphere

Fig. 2.7 shows the reconstructed images of a hollow sphere positioned at the isocenter of three different tomographs: a closed-ring and two dual-head tomographs with different opening angles ϕ (cf. Fig. 2.1). A very high number of annihilations, 100 million (1 MBq cm^{-3}), was simulated in each case in order to exclude possible low statistics artifacts. The images were obtained after 50 iterations with the MLEM algorithm, with a solid angle correction applied to the intermediate image between each iteration step. It can be seen that, as expected, the three views obtained with a closed-ring tomograph are very similar to the originally simulated hollow-sphere, with the activity in the hollow region at the isocenter being as low as approximately 5 % of the maximum, homogeneous activity (although no activity at all was expected here). If a dual-head tomograph with $\phi = 46°$ is considered, corresponding to a length of 34 cm along the Y_{PET} axis without detector coverage, a slight image elongation is observed along this axis, affecting therefore the saggital and transversal views of the image. When the detector gap along the Y_{PET} axis is increased to 63 cm, corresponding to an angle $\phi = 100°$, both the sagittal and transversal views of the image present an extended elongation with, consequently, high loss of image intensity. Furthermore, the frontal view shows an activity in the hollow region at the isocenter of approximately 30 % of the image maximum, therefore disturbing image evaluation in cases where non-expected activity is present in empty cavities.

Based on these sets of images, a dual-head tomograph with small gaps, i.e. $\phi = 46°$, seems to bring an optimum detector configuration for an in-beam PET tomograph since it seems not to induce strong image deterioration nor loss of signal intensity, while offering the advantage of allowing an entrance and escape portal for the incoming beam and outgoing light-particle flux [Gun04a, Gun04b], respectively. Nevertheless, the dimensions of the simulated hollow-sphere, with an outer diameter of 6 cm only, allow this conclusion to be applied to small tumors only. In order to study the same image deterioration effects onto activities positioned further away from the isocenter, the hollow sphere was shifted by 3 cm along the Y_{PET} axis, with results presented in the next section.

2.5.2 Importance of detector geometry over collected statistics

Besides a shift of 3 cm along the Y_{PET} axis, the activity density of the hollow-sphere simulated in the present section was decreased by 2 orders of magnitude, down to 10 kBq cm^{-3} (1 million simulated annihilations), in respect to the case presented in the previous section. This allows to study the performance of the different detector configurations when a low-statistics annihilation activity is further apart from the isocenter. Fig. 2.8 shows the images obtained in the same conditions presented above: after applying 50 iterations to the simulated data with the MLEM algorithm, with a solid angle correction implemented between each iteration step.

It can be seen that the images obtained with a closed ring detector configuration become noisier, as expected due to the lower statistics data sets, but with no influence observed neither in the shape of the activity contours nor in the signal intensity inside the inner empty cavity. In the dual-head, small-gaps detector configuration ($\phi = 46\,°$), the frontal view presents almost the same results obtained with a closed-ring detector configuration. The saggital and transversal

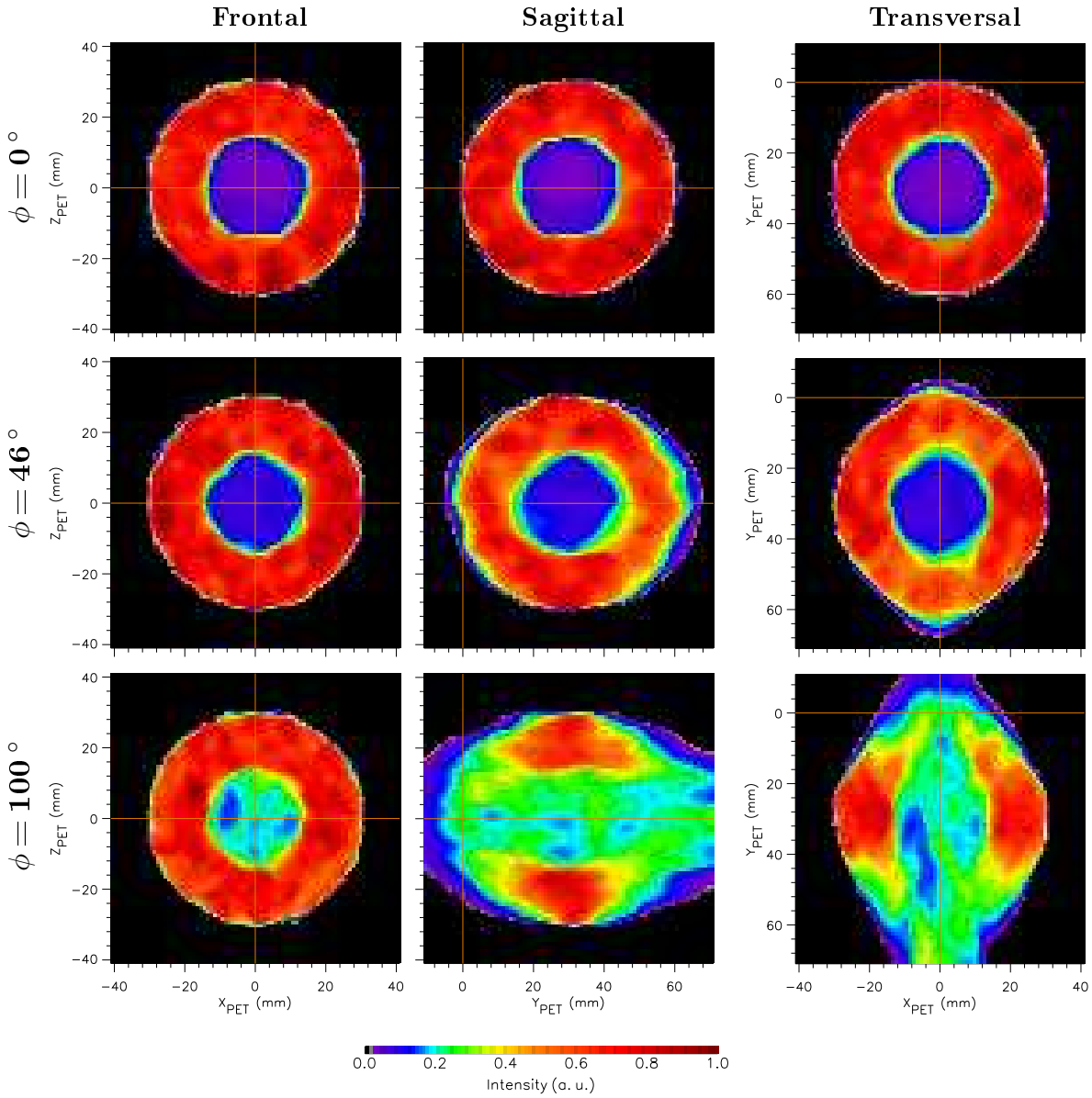

Figure 2.8: Reconstruction of a hollow sphere with low statistics (1 million annihilations simulated) with the center of the sphere shifted 30 mm along Y_{PET}. The number of detected coincidences were approximately 3.2×10^5, 2.3×10^5 and 1.4×10^5 for the detector configuration with $\phi = 0\,°$, $\phi = 46\,°$ and $\phi = 100\,°$, respectively.

image views, however, do present some small loss of signal intensity at the edges of the image along the Y_{PET} axis, with a consequent slight image intensification in the middle of the hollow sphere at $Y_{PET} \sim 30$ mm. This fact, brought to an extreme with the dual-head, wide-gaps detector configuration ($\phi = 100\,°$), is also observed with the realistic patient-treatment images simulated in the next section.

Besides the mentioned loss of signal intensity, the comparison of Fig. 2.8 with Fig. 2.7 allows to conclude that the geometry of the detector configuration plays a much more important role in in-beam PET than the number of collected events, i.e. a low-statistics image acquired with a closed-ring tomograph (Fig. 2.8, top row) contains more information than a high-statistics image sampled with a dual-head detector configuration (Fig. 2.7, middle and bottom rows).

2.6 Tomograph Optimization with Realistic Patient Images

In order to be able to evaluate the quality of the images from several camera configurations in real therapeutic situations, β^+-activity distributions calculated from real treatments were connected to the simulation routine. For that, the PosGen Monte-Carlo code [Has96, Pön04], which generates a β^+-activity distribution for a given carbon ion irradiation field based on the computed tomogram (CT) of the patient and on a particular delivered irradiation, was slightly modified: the spatial coordinates of the generated β^+-activity distribution were saved before taking into account the positron annihilation and the detection of the corresponding γ-rays with the BASTEI tomograph. This generated β^+-activity distribution was then the input of the routine that simulates the three tomograph detector configurations under study. Table 2.2 summarizes the simulation and reconstruction details of sections 2.6.1 and 2.6.2. It can be seen that the activity of the simulated images is one order of magnitude higher than the estimated target activity produced in both treatments considered. This was done in order to study the influence of the detector geometry onto their reconstructed images without influences from low statistics data sets. A low statistics simulation, corresponding to treatment-like data sets, was performed for the head and neck irradiation and results are shown for two tomograph geometries.

Table 2.2: Measured and simulated target activity for the two treatments studied.

Treatment considered	Head and neck	Pelvis
Coincidences detected with BASTEI[a]	1.13×10^5	4.76×10^5
Measuring time (s)	712	860
Effective measuring time[b] (s)	551	529
Estimated average target activity[c] (kBq)	4.1	18
Simulated target activity[d] (kBq)	35	180

[a] Measured in the pauses between beam extraction only.
[b] Measuring time weighted with the accelerator duty cycle delivered.
[c] Assuming an integrated coincidence detection efficiency of 5 %.
[d] High statistics data sets. Low statistics (text) denote one order of magnitude less.

2.6.1 Head and neck irradiation

High statistics simulated data sets

Fig. 2.9 depicts a typical portal for a head and neck irradiation with carbon ions. The images in the top row show the delivered physical dose generating a given β^+-activity distribution, shown in the bottom row. Both the physical dose and the β^+-activity distribution are superimposed onto the CT of the patient. In the case shown, the beam enters the patient from the left (right in the frontal and transversal images) forming an angle of 14° clockwise with the X_{CT} axis, as can be seen in the frontal view. The transversal view allows to see that the patient head is tilted to the left (right in the image). As expected, a good agreement between the generated β^+-activity distribution and the anatomical structures of the patient, e.g. the sinus cavities, is observed, with an enhanced activity concentration generated in higher density target structures like bone. This last detail is further increased in real patient images due to biological mechanisms like washout, diffusion or transport of the β^+-activity by the blood circulation or by highly perfused tissues. These metabolic processes were not included in the images shown since the PosGen Monte-Carlo code does not simulate them yet.

By simulating the detection of the β^+ activity distribution displayed in the bottom images of

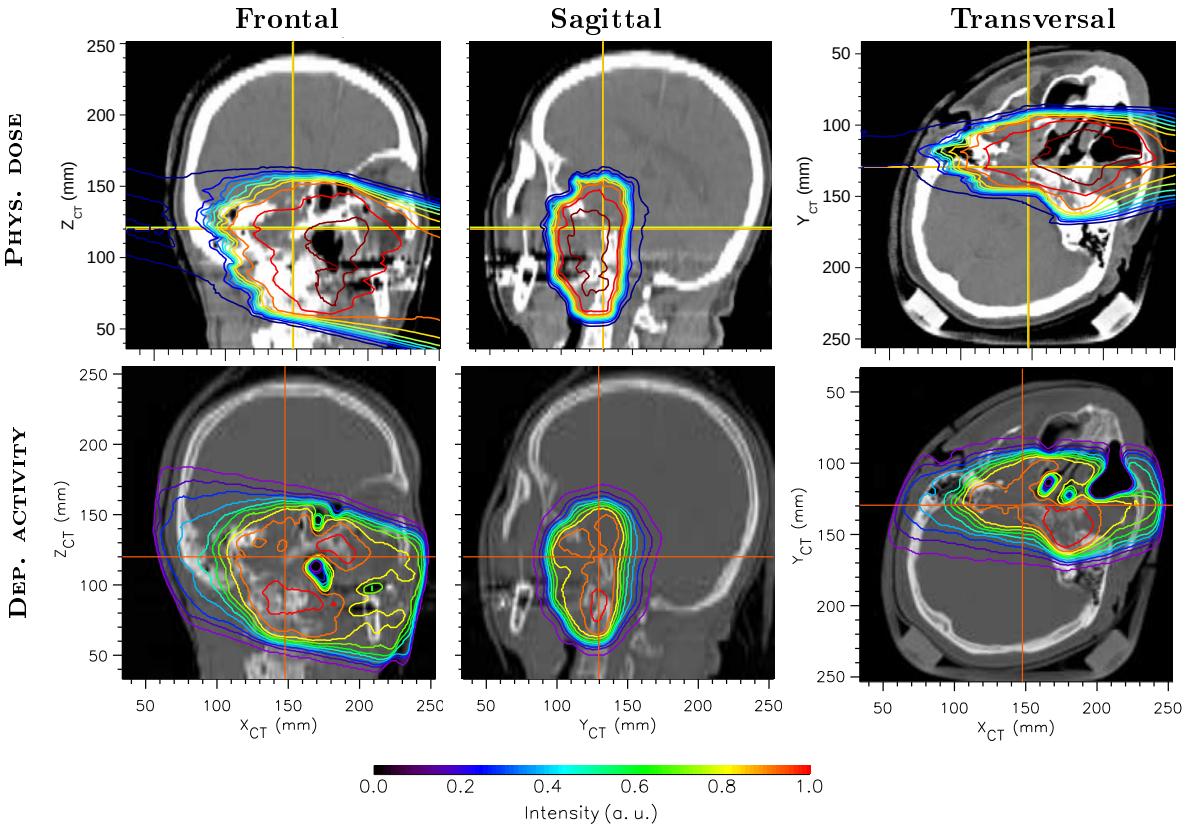

Figure 2.9: Head and neck irradiation: physical dose and generated β^+ activity distribution. Iso-dose (top) and iso-activity (bottom) contours are superimposed onto the patient CT.

Fig. 2.9 with the three different detector geometries under study the reconstructed images of Fig. 2.10 were obtained. For the closed-ring detector geometry the simulated positron camera was rotated around the Y_{PET} axis by 6° anti-clockwise, i.e. the X_{CT} and X_{PET} axes form an angle of 6°, with the beam direction and the X_{PET} axis forming an angle of 20°. In the case of both dual-head detector configurations the simulated positron camera was rotated 14° clockwise so that the beam crosses the camera through its midplane, along the X_{PET} axis.

The images obtained with the closed ring tomograph are remarkably similar to the β^+-activity distribution displayed in Fig. 2.9. This was expected since, despite the rotation of the camera in respect to the beam direction, the FOV of the camera covers all the irradiated volume. It can be seen that important characteristics for clinical in-beam PET are well conserved: (1) a sharp activity gradient is observed at the distal edge of the irradiation field in the frontal and transversal views (distal contours with values between 90 % down to 40 % of the maximum activity, approximately), which allows to monitor the range of the treatment field; (2) a good overlap exists between the patient empty cavities, like the maxillary and ethmoid sinuses and the mouth cavity, with the minima of the β^+ activity (frontal and transversal views); (3) the activity maxima are localized in the same bone structures obtained with the PosGen code (all views); and (4) the outline of the activity contours matches well that obtained with the PosGen simulation in all image views.

The reconstructed images obtained with a dual-head tomograph with narrow gaps ($\phi = 46\,°$) are similar to the closed-ring ones in what concerns variables (1), (2) and (4) mentioned above. However, a shift in the activity contour with maximum intensity is observed, which is thought to arise from the asymmetric loss of image intensity at locations not equally distant from the

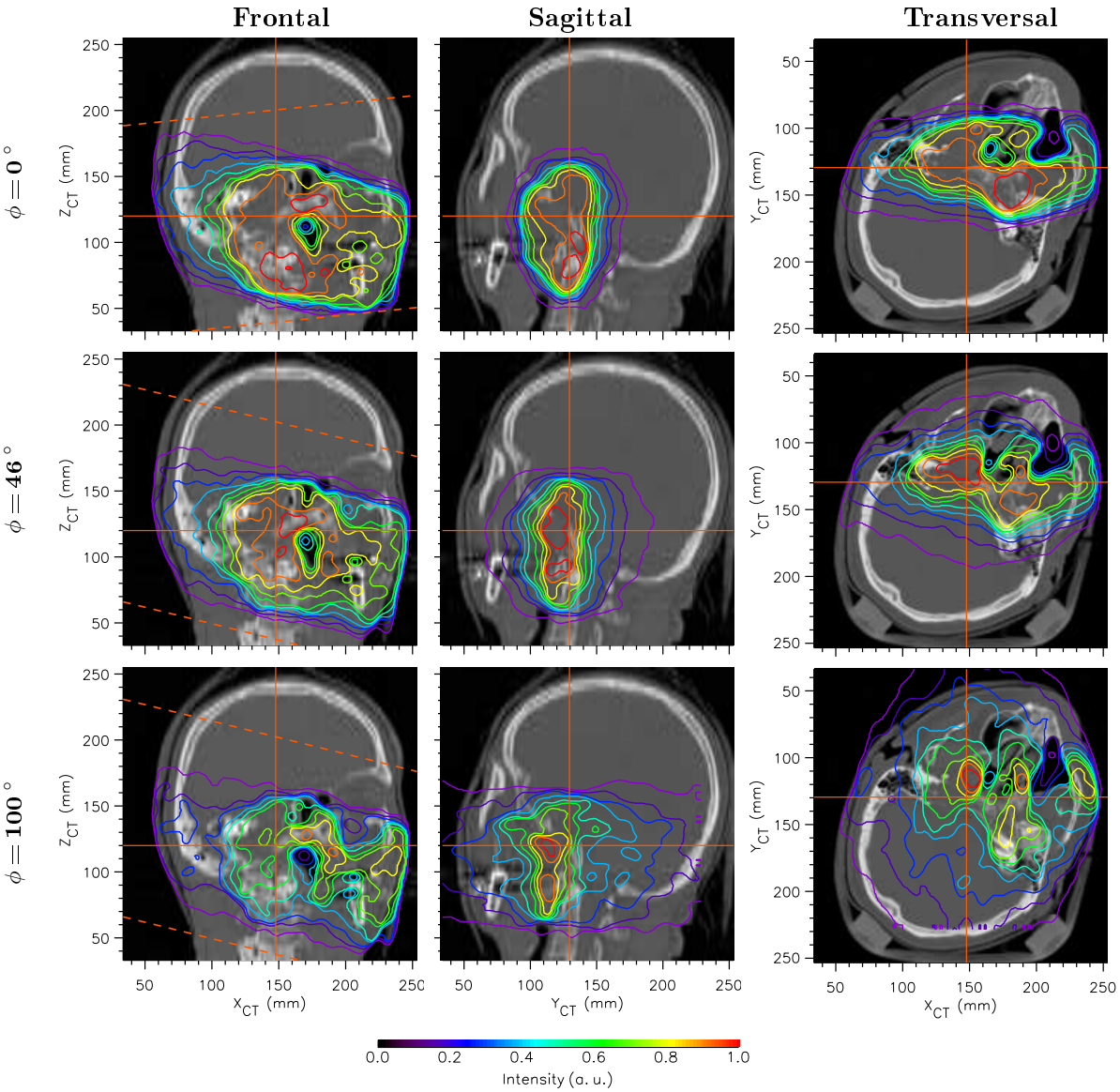

Figure 2.10: Head and neck irradiation: reconstruction with different tomographs. The dashed lines in the frontal views depict the margins of the tomograph considered (top view).

isocenter, as detailed in Fig. 2.8. Nevertheless, the quality of the reconstructed images shown seems to be quite high for monitoring tumor irradiation.

In what concerns the dual-head tomograph with wide gaps, $\phi = 100\,°$, the reconstructed images show the expected object elongation along the Y_{PET} axis (overlapping the Y_{CT} axis). In addition, the frontal and transversal views show the effect detailed in Fig. 2.5, where a noisy activity signal corrected with too low solid angle values gives rise to a false increase in signal intensity. It must be stated that these images cannot be directly compared to those obtained with the BASTEI tomograph. Besides the different detector geometries, spherical in BASTEI versus cylindrical in the present studies, the reconstruction routine developed for BASTEI uses a dedicated penalization algorithm for image coordinates located too far apart from the isocenter, therefore maintaining image proportionality in regions surroundoing the isocenter, where the tumor is located. Nevertheless, the present images do show that items (1) and (2) mentioned above are still valid, meaning that monitoring the irradiation range and possible patient morphological alterations is still possible with accuracy with the present images.

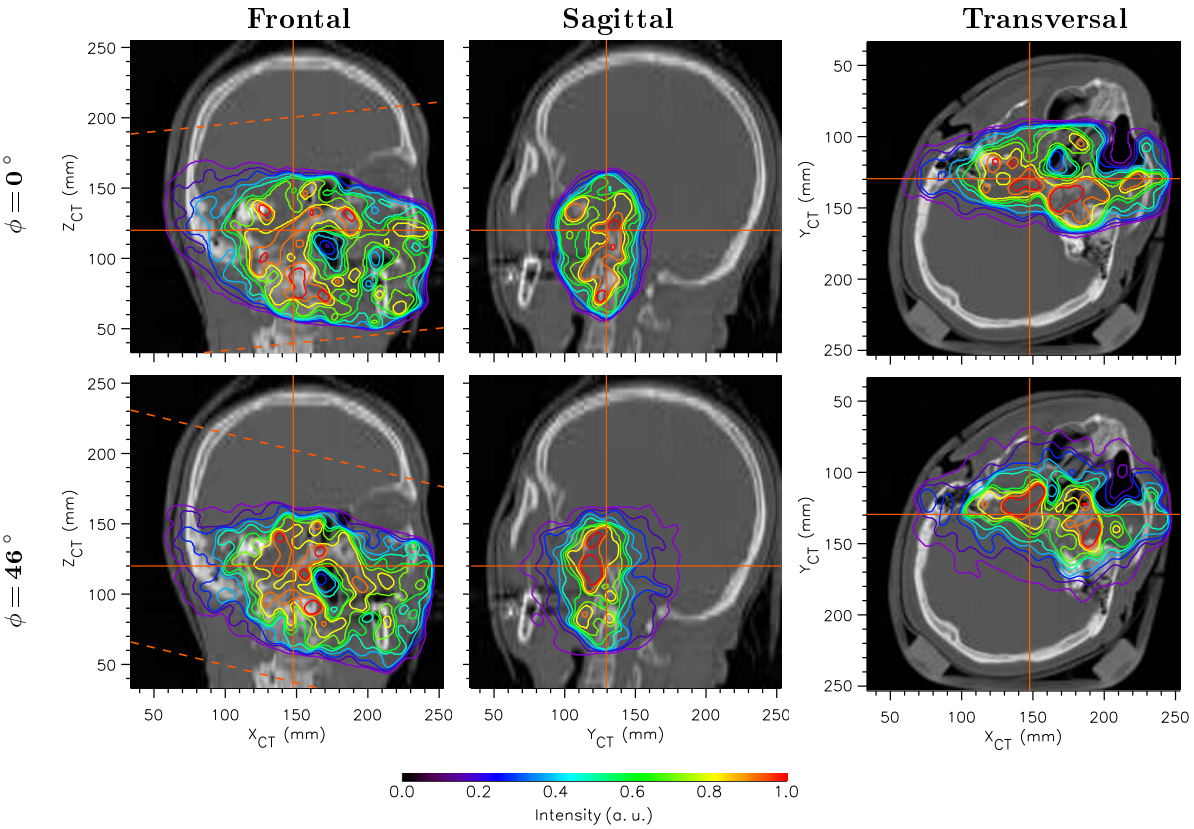

Figure 2.11: Head and neck irradiation: study with low statistics data sets. A total of 2.5 million simulated annihilations yielded 2.4×10^5 and 1.75×10^5 events detected with the closed ring and the dual-head tomographs, respectively. The dashed lines in the frontal views depict the margins of the tomograph considered (top view).

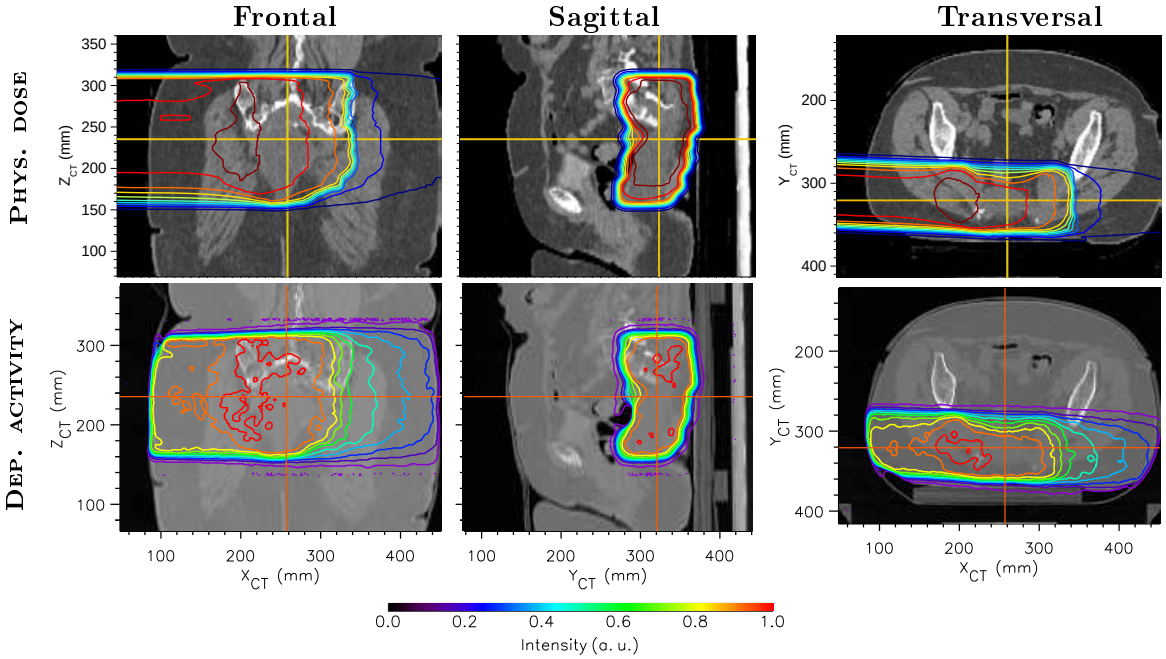

Figure 2.12: Pelvis irradiation: physical dose and generated β^+ activity. Iso-dose (top) and iso-activity (bottom) contours are superimposed onto the patient CT.

Low statistics simulated data sets

Fig. 2.11 shows that, for the closed-ring and dual-head, small-gaps tomographs, the conclusions obtained with the higher statistics data sets in Fig. 2.10 are still valid if more realistic, low statistics simulations are taken into account. Despite the higher noise (granularity) of the images in respect to the high statistics images of Fig. 2.10, mostly observed for the maximum β^+-activity contours, the agreement of the remaining iso-activity lines with the simulated, deposited activity is still valid, namely the sharp activity gradient at the distal edge of the irradiation field, the overlap with empty patient cavities and the overall agreement of the outline of the activity contours with the predicted contours.

In summary, it is evident that a closed-ring tomograph conserves all important characteristics from clinical in-beam PET. For the irradiation of head and neck tumors a dual-head tomograph with small gaps ($\phi = 46\,^\circ$) maintains most of the characteristics of in-beam PET needed for clinical use meaning that, should the installation of a closed-ring detector geometry be not feasible, the dual-head geometry with $\phi = 46\,^\circ$ should be preferred in respect to the geometry with $\phi = 100\,^\circ$. The feasibility of implementing a closed-ring tomograph is studied in section 2.7.

2.6.2 Pelvis irradiation

Spinal chordomas cannot be treated with an effective dose using conventional radiation therapy without exceeding the tolerance dose of the spinal cord while ensuring sufficient target coverage at the same time [Sch03a]. For this reason, several patients suffering from the mentioned tumors have been irradiated with carbon ions at the GSI pilot facility, within a treatment complemented with fractionated irradiation with photon intensity modulated radiation therapy (IMRT). Fig. 2.12 depicts one fraction of a carbon ion pelvis irradiation as mentioned. In addition to continue treating spinal chordomas, the dedicated facility in Heidelberg will also exploit the advantages of heavy ions to treat patients suffering from prostate cancer [Nik04]. In both cases, and in other tumors outside the head and neck region that are planned to be addressed at a later stage, monitoring the heavy ion irradiation with in-beam PET brings usefull information to the radiotherapist due to the close proximity of organs at risk (OAR) to the target volume. In the sagittal view of Fig. 2.12 it can be seen that the colon of the patient, a radiosensitive organ, lies adjacent to the target volume. The present section studies the influence of the detector geometry onto in-beam PET images in this situation.

By simulating the detection of the β^+-activity distribution shown in the bottom row of Fig. 2.12 with several tomographs the reconstructed images of Fig. 2.13 were obtained. For the closed-ring configuration ($\phi = 0\,^\circ$) two detector arrangements were considered: a large coverage ring with 24 cm axial FOV, 45.6 cm inner radius and rotated 18° clockwise around its Y_{PET} axis, thus allowing a collision-free beam delivery (top row); and an ECAT EXACT HR$^+$-like geometry with the tomograph rotated 25° clockwise around its Y_{PET} axis (second row) for the same reason. Clearly, the large coverage closed-ring configuration yields the best images and in section 2.7 its implementation feasibility is discussed. Nevertheless, although the smaller closed-ring tomograph considered does not cover the proximal and distal irradiated volume completely, the images corresponding to the covered regions do resemble remarkably well the generated β^+-activity. It can be seen that the reconstructed distal edges of the activity allow to monitor the range of the irradiation by direct comparison with the simulated activity contours (frontal and transversal views) and, in addition, the sharp activity gradient observed in the saggital view allows a precise monitoring of the irradiation close to the colon of the patient, in this case.

Although the FOV of both dual-head tomographs ($\phi = 46\,^\circ$ and $\phi = 100\,^\circ$) cover the irradi-

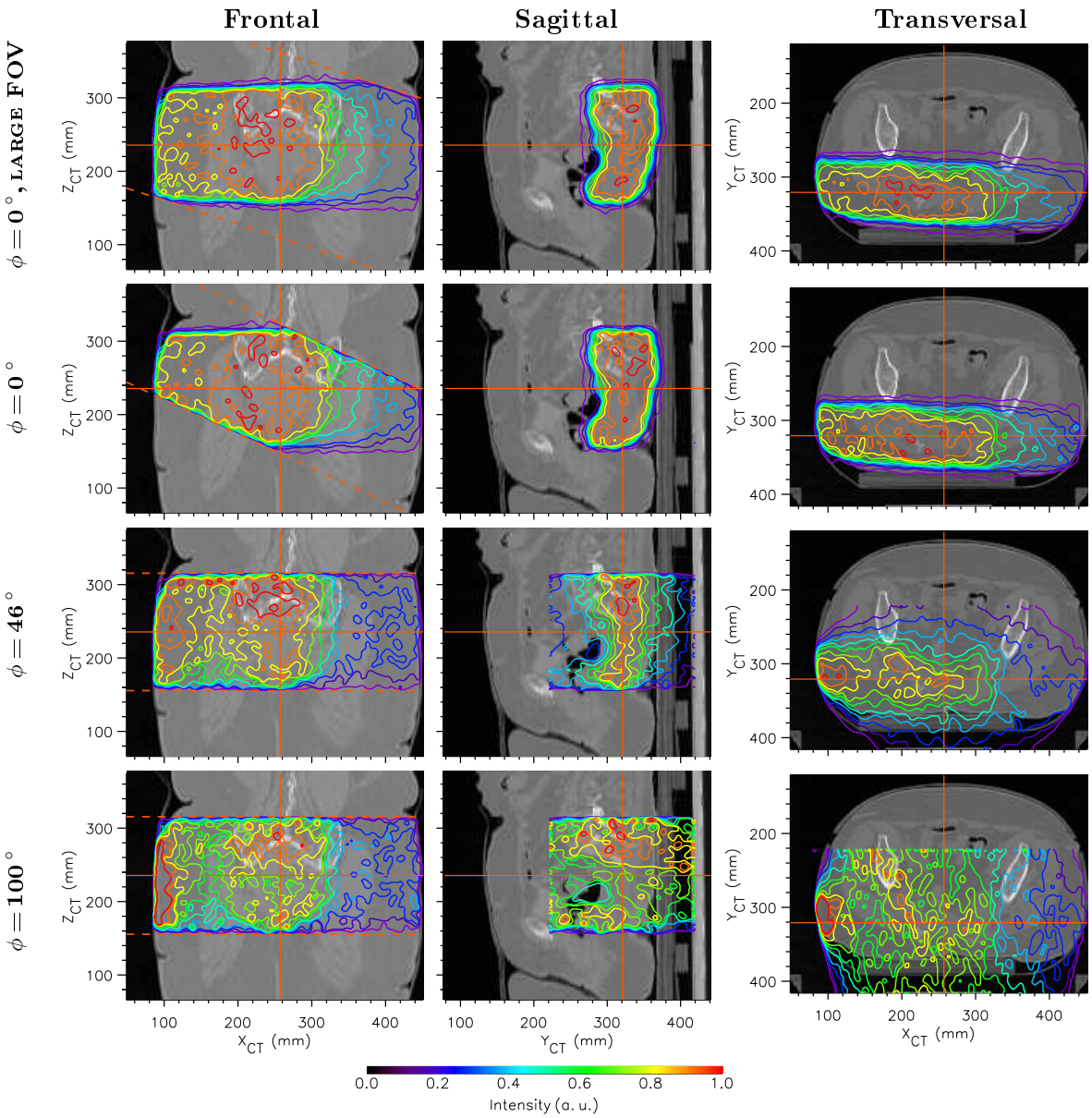

Figure 2.13: Pelvis irradiation: reconstruction with different tomographs. The dashed lines in the frontal views depict the margins of the tomograph considered (top view). The top row shows images obtained with a simulated tomograph with an axial FOV (a) of 24 cm and radius (R_{PET}) of 45.8 cm; in the remaining an ECAT EXACT HR$^+$-like scanner was considered: $a = 16$ cm and $R_{PET} = 41$ cm.

ated volume completely, their reconstructed images contain clearly less information as that obtained with a rotated closed-ring tomograph due to the image degradation arising from the gap between the detector heads (section 2.5).

In summary, for large irradiation fields occuring during tumor treatments in the pelvis region, in-beam PET benefits the most from a closed ring tomograph. It was seen that even a cheaper solution, like a commercially avaliable, conventional nuclear medicine scanner with approximately 16 cm axial FOV, yields better image quality as any fixed, dual-head tomograph, despite the incomplete coverage of the irradiated region in the case of the closed-ring geometry. The best images were obtained with a large FOV tomograph and the next section studies the feasibility of its implementation.

2.7 Feasibility of a Closed-Ring In-Beam PET Scanner

Due to the higher image quality obtained with a closed-ring tomograph, particularly with large irradiation fields, the present section investigates the possibility of implementing such an in-beam PET scanner for heavy ion tumor irradiation. The top images in Fig. 2.14 depict a worst-case irradiation scenario: a beam portal with maximum beam width and delivered perpendicularly to the patient. Assuming a rotation of the tomograph around its Y_{PET} axis, as depicted in the top-right image, the maximum beam radius R_b that does not collide with the in-beam PET detectors is given by

$$R_b = \sqrt{R_{PET}^2 + (a/2)^2} \cdot \cos\left[\arcsin\left(\frac{D}{2 \cdot \sqrt{R_{PET}^2 + (a/2)^2}}\right) + 2 \cdot \arctan\left(\frac{a}{2 \cdot R_{PET}}\right)\right], \quad (2.3)$$

with R_{PET} the inner radius of the tomograph, D the diameter of a cylinder-shaped volume reserved for the patient and couch and a the axial FOV of the tomograph. The graphs in the bottom of Fig. 2.14 depict both the correlation between R_b and a, from Eq. 2.3, for two tomographs with different R_{PET} (solid curves, left Y axis), as well the correspondence between d_n and a (dashed curves, right Y axis). It can be seen that a tomograph with e.g. $R_{PET} = 45.8$ cm and $a = 24$ cm (Fig. 2.13, top row) can be implemented with a patient table not wider than 65 cm (the maximum width at the GSI facility) provided that the center of the tomograph is aligned with the central axis of the patient table and that the distance between

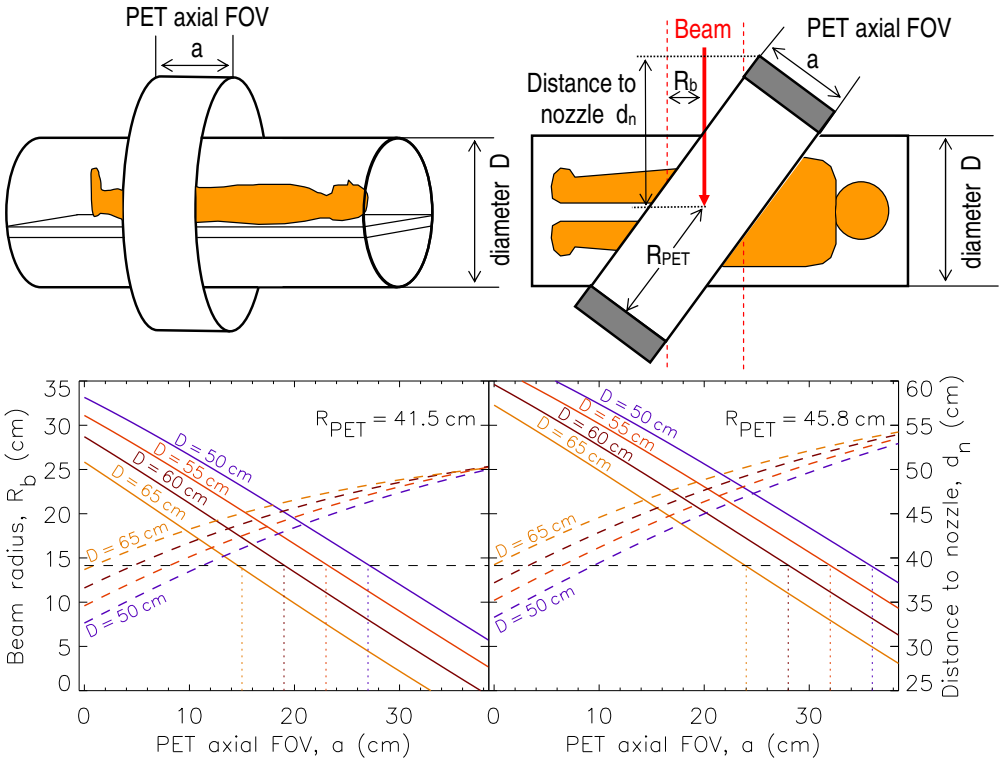

Figure 2.14: Feasibility of a closed-ring, in-beam PET tomograph with inner radius R_{PET}. The correlation between the maximum allowed beam radius R_b (left Y axis) and the axial FOV of the tomograph a is plotted with solid lines. The dashed lines plot the distance of the isocenter to the nozzle d_n (right Y axis) versus a for a scanner with 5 cm radial depth. The dashed line at $R_b = 14.14$ cm denotes the radius of a circle containing the maximum beam window deliverable at the GSI facility ($20 \times 20\,\mathrm{cm}^2$).

the nozzle and the isocenter is not smaller than 50 cm. This last result assumes an in-beam PET scanner with a radial depth of 5 cm, a technological challenge since these 5 cm should include the detectors, front-end electronics and cabling as well as the support structure. Nevertheless, an existing solution has been developed for the PEM dual-head tomograph [Var05] which satisfies these restrictions[1].

2.8 Summary and Outlook

A fully 3D, maximum likelihood expectation maximization algorithm applicable to several closed-ring or dual-head tomographs was developed. It complements the reconstruction routine previously developed for the limited angle in-beam positron tomograph installed at the GSI tumor therapy facility. The combination of the new routine with a software package simulating different detector arrangements, also developed within this work, allowed the degradation of PET images obtained with dual-head tomographs to be quantified. It was seen that a smooth spatial distribution of the coincidence detection efficiency of a tomograph is highly desirable in order to reduce artifacts arising at the edges of the efficiency-corrected images, namely a false increase of image intensity if no image penalization is applied. Another image artifact arising with dual-head tomographs is the degradation of the spatial resolution of the image in the axis along the detector gap, leading to signal loss along that axis.

The evaluation of images obtained from simulated, real patient treatments for a head and neck and a pelvis irradiation revealed that a dual-head tomograph with an opening angle of approximately 46° yields satisfactory results in the case of the head and neck irradiation (smaller target volume). As expected, the best image quality was obtained with a closed-ring tomograph. Even with an incomplete coverage of the irradiated volume in the case of the pelvis treatment, the reconstructed β^+-activity distributions are remarkably similar to that generated in the patient. For this reason, the feasibility of implementing a closed-ring, in-beam PET scanner was investigated. It was seen that, considering the dimensions of the patient table and maximum beam window at the GSI facility, the installation of such a tomograph is possible, provided that the isocenter of the tomograph is aligned with the central axis of the patient table during the measurements. This last detail means that the isocenter of the target volume may not correspond to the isocenter of the in-beam PET scanner. As seen, this does not impose a loss of image quality for a closed ring tomograph and offers, in fact, two advantages: (1) increased simplicity, in respect to a target-isocenter fixed solution, in the process of bringing the tomograph into the measuring position and, (2) availability of radiotherapy monitoring by means of in-beam PET to all patients with a maximum width of 65 cm, independently of the location of their tumor. Item (2) cannot be satisfied with a dual-head tomograph since both isocenters, those of the tomograph and of the target volume, must overlap during the irradiation due to the image degradation seen at locations far from the isocenter of the tomograph. The integration of an in-beam PET scanner onto a rotating beam delivery is discussed in chapter 3.

Finally, it must be stated that the reconstruction routines developed provide a working solution for whatever tomograph found to be optimum for next-generation, in-beam PET systems. Nevertheless, their merging with modern, faster algorithms, e.g the ordered subsets expectation maximization (OSEM), typically reducing the number of iterations from 50 to only a few, is highly desirable in order to significantly decrease the data processing time.

[1] The prototype LSO/APDA PEM detectors, with a radial depth of approximately 4 cm, include two APDA per scintillator (DOI-PET), the corresponding fast readout electronics and cabling as well as the mechanical support structure.

Chapter 3

Integrating In-beam PET into Horizontal and Isocentric Ion Beam Deliveries

3.1 Motivation

The clinical results achieved by the pilot project at the tumor therapy unit at the Gesellschaft für Schwerionenforschung (GSI) in Darmstadt have prompted the construction of a dedicated, hospital-based facility [Hea98] providing much higher patient throughput by implementing three treatment rooms (beam deliveries). One of these will be equipped with an isocentric beam delivery (gantry) offering almost no restrictions in beam portal selection, i.e. close to fully 3D beam entrance coverage. This was seen to bring clinical advantages for treating more delicate therapeutic situations [Jäk00]. For this reason, an in-beam positron tomograph is planned to be installed in this treatment room. This fact has prompted research activites in order to (1) satisfy the technical restrictions imposed by medical needs and by all operating equipment to be installed at this isocentric beam line and (2) optimize this next-generation, in-beam tomograph by studying and minimizing the limitations of the presently operating in-beam scanner BASTEI.

Concerning in-beam PET integration, i.e. item (1) above, the technical restrictions are six-fold: (1) fast accessibility of the medical personnel to the patient at all times (this chapter); (2) collision-free solution concerning in-beam PET, beam nozzle and patient and couch (this chapter); (3) collision-free solution concerning in-beam PET and the incoming and outgoing [Gun04a, Gun04b] particle flux (sections 2.7 and 5.3); (4) volume minimized tomograph due to integration reasons (chapter 4); (5) magnetic field insensitive detectors due to the close proximity, at different distances and changing beam energies, of the last beam bending magnet (section 4.2.2); and (6) state-of-the-art detectors providing optimum γ-ray detection efficiency as well as energy and time resolutions for an efficient suppression of the high-yield, in-beam induced event background (chapter 6). In what regards the optimization of the tomograph itself, i.e. item (2) in the previous paragraph, the studies in chapter 2 showed that a closed ring detector geometry yields the best quality of in-beam PET images, followed by a small-aperture, dual head tomograph. For this reason, the implementation of these two tomograph configurations onto an isocentric ion beam delivery (gantry) are studied in the present chapter.

3.2 The Collision Table Between Gantry and Patient Table

A study analyzing the treatment of tumors under more delicate therapeutic situations, due to the close proximity of organs at risk (OAR), revealed that an isocentric beam delivery (gantry) offering almost no restrictions in beam portal selection brings important clinical advantages [Jäk00]. It was seen that all positions of the ion gantry and patient table that do

not lead to a physical collision between them constitute a desired beam portal. In Fig. 3.1 the coordinate system used[1] is described, together with a so-called collision table which correlates gantry and patient table angles, allowing to know at a glance whether a given combination of gantry and table angles yields a physical collision between them or constitutes an allowed beam portal. It can be seen that the collision areas signed correspond to beam portals where the irradiation would arrive to the patient in an approximate caudo-cranial direction (from the feet up) and would not be included, consequently, in a feasible treatment plan. All gantry-table angle combinations not signed are free for patient irradiation.

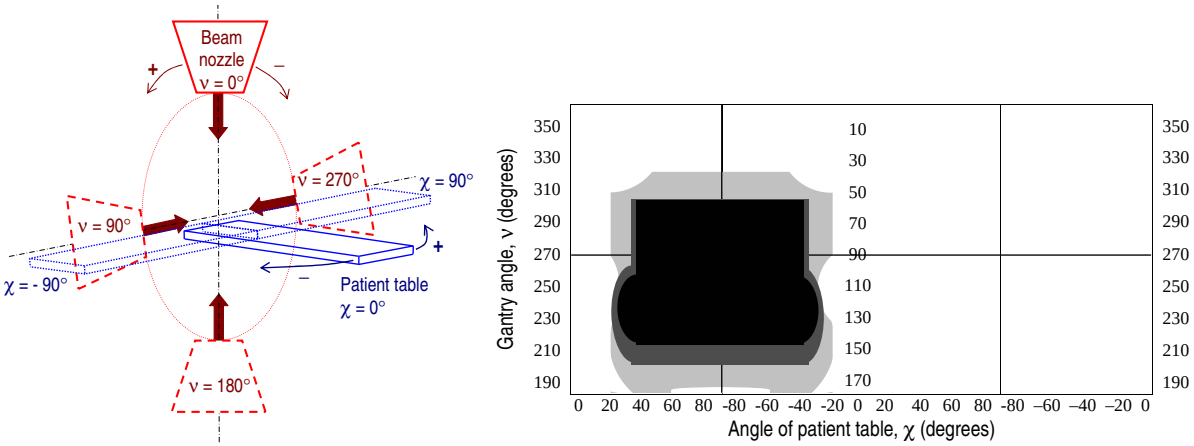

Figure 3.1: Coordinate system for the beam nozzle and patient table angles (left), according to the IEC[1] coordinate convention [Joy74], and corresponding collision table (right). The middle quadrants in the collision table correspond to gantry angles ν between 0 and 180°, as shown in the corresponding ordinate axis plotted at the center. The outer quadrants (first and fourth) correspond to ν between 180 and 360° (ordinate axis at the edges). The black and dark gray areas in the collision table correspond to nozzle and patient table angle combinations resulting in a physical collision between both. The different areas arise from different sizes of the patient table and couch considered. If a linear accelerator-based facility is considered the light gray area results [Jäk00].

In the following sections the integration of an in-beam PET scanner into the treatment room equipped with the ion gantry is studied. For every integration possibility analyzed a collision table was constructed, marking those angle combinations that lead to either some physical collision of the PET scanner with any other instrument, or a collision of the incoming/outgoing beam with the material of the PET scanner. The best integration design should not increase the collision area signed in Fig. 3.1.

3.3 PET at the Patient Couch

In this configuration, illustrated in Fig. 3.2, the tomograph is installed with its rotation axis parallel to the patient table. The dual-head PET scanner moves along the couch and can be positioned around the region being irradiated, with the aperture between the two detector heads allowing the beam to pass through without touching the γ-ray detectors (not shown in the right image in Fig. 3.2). This configuration can provide a full coverage of the volume under observation if the detector heads are allowed to rotate around its axial direction (Z_{PET} in

[1] Every beam input direction corresponds to a combination of patient table and beam gantry angles. Herein the angles are stated according to the Internationl Electrotechnical Commmision (IEC) coordinate convention [Joy74].

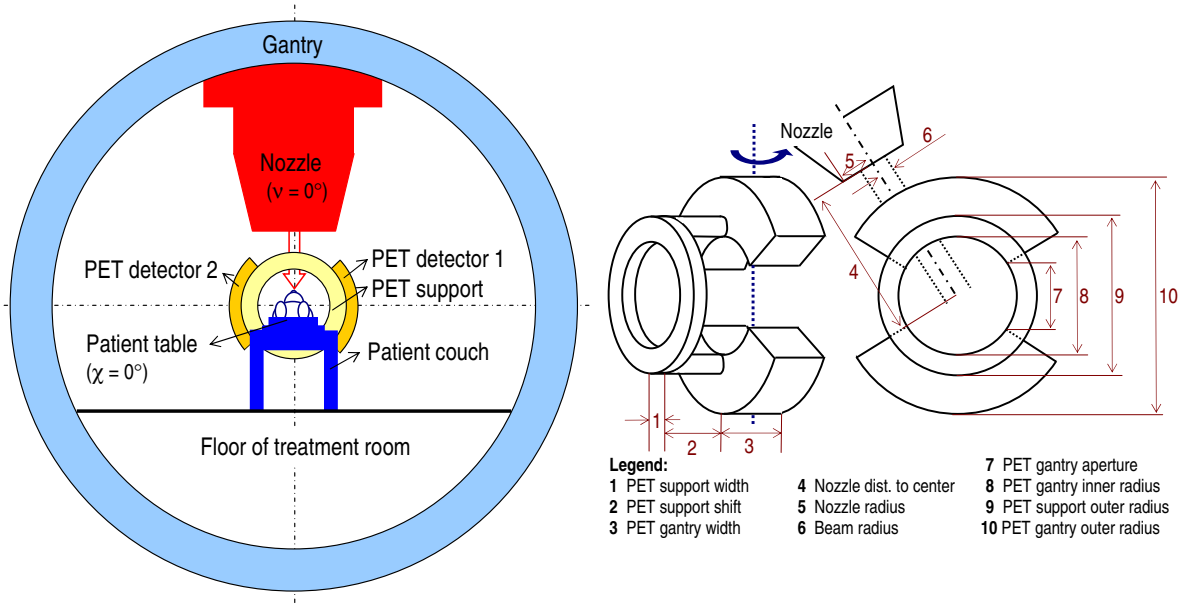

Figure 3.2: PET at the patient couch. A dual-head positron scanner is fixed to the patient couch with its axis parallel to that of the patient table. The detector heads rotate, based on their support ring, allowing the aperture between them to be positioned along the beam (not shown in the right image).

Fig. 2.1) provided that the rotation movement is correlated with the beam delivery macropulses so that no detector lies in the beam path during particle extraction. Such solution requires most probably complex stability issues to guarantee that the moving detector heads do not shift the isocenter of the in-beam positron tomograph. Another possibility to provide full coverage of the irradiated region arises by tilting a closed-ring tomograph, as proposed in section 2.7. This is feasible in the present configuration provided that the tomograph is allowed to rotate

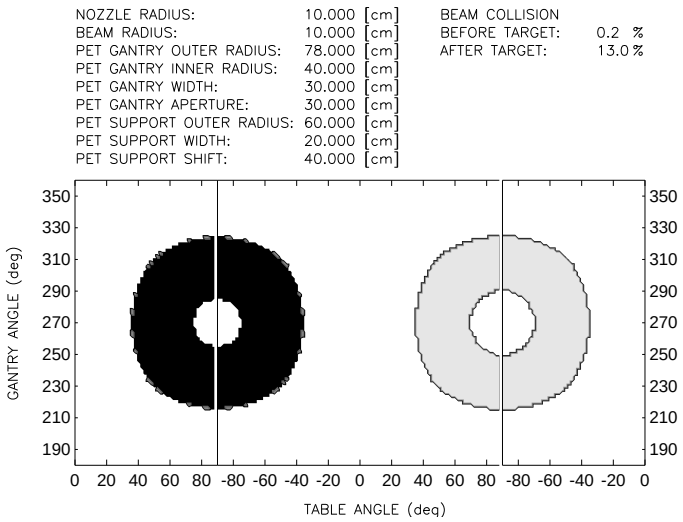

Figure 3.3: Collision table for the configuration with PET at the patient couch. Calculated both for a closed ring as well as a dual-head tomograph. The dark area denotes a physical collision between the nozzle and the support ring of the PET scanner. It lies within the caudo-cranial portals that are not used. The gray area signs a collision of the particle flux leaving the patient, downbeam, with the support ring (text has details).

about the axis signed with the dotted line in Fig. 3.2. Fig. 3.3 shows the collision table resulting from the implementation of either a closed ring or a dual-head tomograph at the patient couch. The dimensions of all components signed in its legend were optimized in order to achieve the minimum collision area. It can be seen that 13 % of all possible portals would result in an irradiation, after the target, of the support ring holding the detectors. This collision area was calculated conservatively, assuming a straight forward propagation of the particle flux downbeam and with a beam radius of 10 cm, as detailed in the Fig. More importantly, the forbidden portals lie exactly in the cranio-caudal direction (from the head down), a favorite and important region of input portals for head and neck irradiation [Jäk00].

In summary, the most important disadvantage of the present configuration is the forbidden irradiation area in the cranio-caudal direction arising from the interaction of the particle flux leaving the patient [Gun04a, Gun04b] with the support of the PET scanner.

3.4 PET on a Separate Gantry

If the PET scanner is fixed on a separate gantry, positioned inside the treatment room and opposite to the patient couch [Eng03] as depicted in Fig. 3.4, than all portals corresponding to the free area in Fig. 3.1 become available. This means that all irradiation fields are possible from the point of view of PET, so that the fobidden portals in the collision table result only from physical collisions between the nozzle and the patient table or couch, as shown in Fig. 3.1. This solution, implementable only with a dual-head tomograph, requires the patient to be positioned for irradiation in a first step, followed by the movement of the PET scanner onto its measuring position in a second step and, finally, the rotation of the ion gantry untill the desired angle ν is reached, i.e. the only extra procedure in respect to the present irradiation at GSI arrives from the moving of the ion gantry. Nevertheless, the positioning of the positron tomograph requires an extra coordination of several synchronous movements signed with the marked block

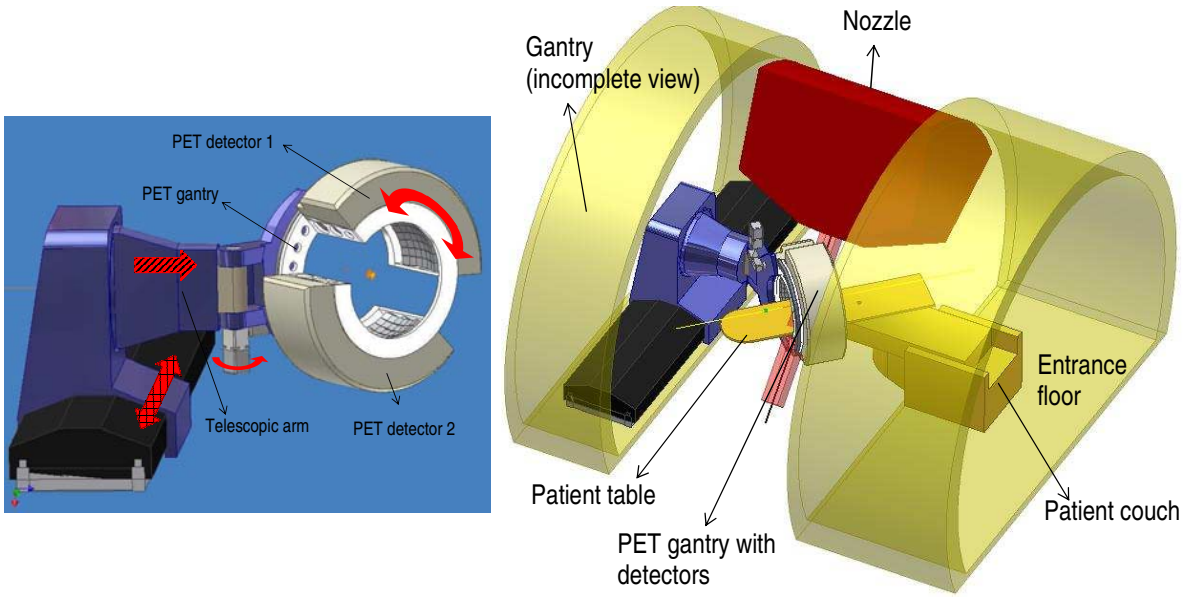

Figure 3.4: PET on a separate gantry. A dual-head positron scanner is fixed on a separate gantry, positioned inside the treatment room and opposite to the patient couch. The patient is first positioned for treatment, followed by the positioning of the dual-head scanner with movements indicated with the block arrows in the left image (text has details).

arrows in Fig. 3.4. These are (1) the extension of the telescopic arm (hashed arrow) in parallel with (2) a dislocation of the arm structure perpendicularly to the movement of arm extension (squared arrow). The synchronization of these movements can be implemented either at the machine level or require human intervention. In either case, a physical collision between the positron gantry and the patient or table during this positioning procedure is not excluded in the case of machine or human error. Such collision possibility is highly minimized with the present PET scanner positioning scheme at the GSI horizontal, fixed beam line. This item constitutes the main disadvantage of the present configuration, together with the time required to bring the PET scanner into its measuring position and, more importantly, the time needed to gain access or release the patient being treated in the case of an emergency.

3.5 PET at the Beam Nozzle

This configuration was developed at GSI for a dual-head tomograph [Kop04]. A support ring, rotating around the nozzle, holds two mechanical arms which position the PET detector heads at the isocenter (Fig. 3.5). During patient positioning the detector heads lie behind (following the beam direction) the support ring (not shown), enabling full patient access at the isocenter. This PET positioning mechanism offers the advantage that, in the case of an emergency during irradiation, the arms open and return the detector heads to their back position without any physical collision being possible neither with the patient or table nor with the nozzle or beam. Therefore, an immediate access to, or release of the patient is possible. In addition, by rotating the two detector heads around an axis perpendicular to the beam direction, shown with the block arrow and dotted line in Fig. 3.5, the implementation of a closed-ring tomograph becomes feasible for all irradiation portals, i.e. the collision table of Fig. 3.1 is valid. This closed-ring tomograph is still divided in two detector heads but without an aperture between them.

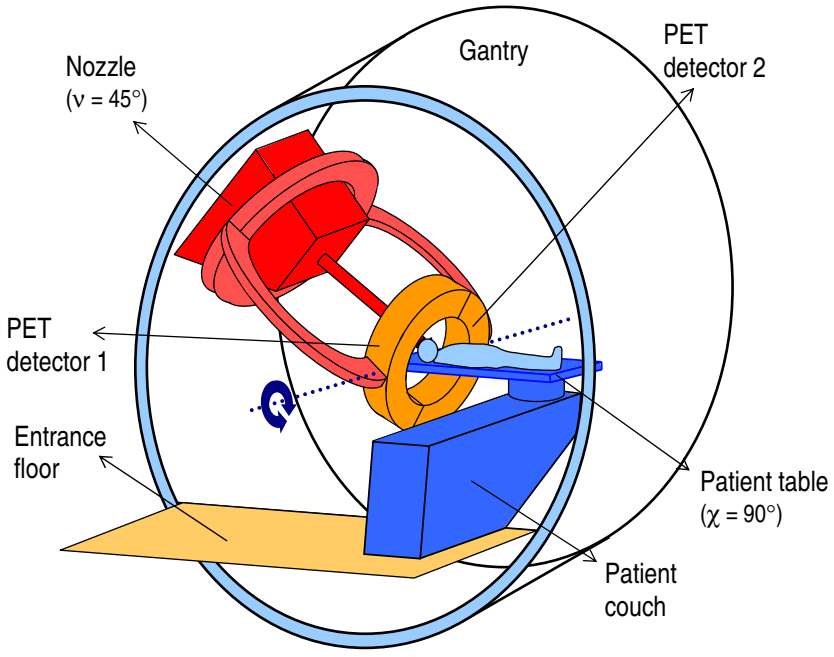

Figure 3.5: PET at the beam nozzle. A support ring rotating around the nozzle holds two arms that position each of the PET detector heads at the isocenter. By rotating the two detector heads around an axis perpendicular to the beam direction (block arrow and dotted line) the implementation of a closed ring tomograph becomes feasible for all irradiation portals.

In summary, the present configuration seems to satisfy all requisites for in-beam PET: a fast access of the medical personnel to the patient at all times; a collision-free solution concerning the PET scanner, the nozzle and the patient and couch with, in addition, no possible interference of the in-beam PET detectors with the beam; and, very important for the quality of in-beam PET images, the implementation of a closed ring detector geometry becomes feasible. On the other hand, some disavantages are brought up by bringing the PET detectors close to the last beam bending magnet, in addition to operating them at different magnetic field strengths during patient irradiation. These issues and their solution are addressed in chapter 4.

3.6 PET at a Fixed, Horizontal Beam Line

Fig. 3.6 displays a solution for implementing a closed-ring, in-beam PET at a fixed, horizontal beam line. It is similar to the present implementation of BASTEI in the sense that the mechanical structure holding the two PET detector heads moves along the beam nozzle, bringing the tomograph into the measuring position and back. The main difference lies in the capability of rotating each detector head about a vertical axis (white arrows in the right image of Fig. 3.6), therefore allowing the tomograph to be placed at the isocenter in a tilted position with respect to the incoming beam. This rotation, together with the vertical movement of each of the mechanical arms holding the two detector heads, allows a closed ring positron tomograph to be installed if the dimensions considered in section 2.7 for the in-beam PET detectors, patient table and distance to nozzle are taken into account.

Should the installation of a closed-ring, in-beam PET be not feasible, a dual-head tomograph with small gaps, installed with the system depicted in Fig. 3.7, is also possible. This tomograph should be built in a way to allow a closed-ring detector configuration to be used whenever possible. Either with a closed-ring or with a dual-head tomograph, the positioning system depicted in Figs. 3.6 and 3.7 offers the advantage of a fast, collision-free access to the patient at all times. For that, the heads just need to be moved apart vertically in the case of an emergency.

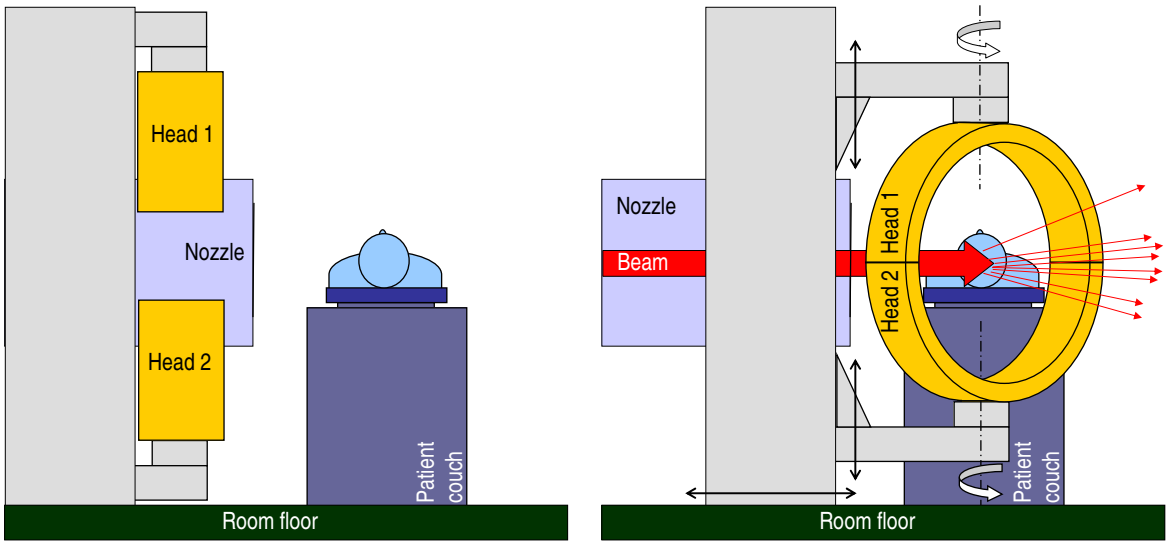

Figure 3.6: Closed ring, in-beam PET at a fixed, horizontal beam line. The left image shows the two detector heads in the park position, whereas in the right the heads are positioned for data taking during irradiation, with the couch at an angle $\chi = 90°$.

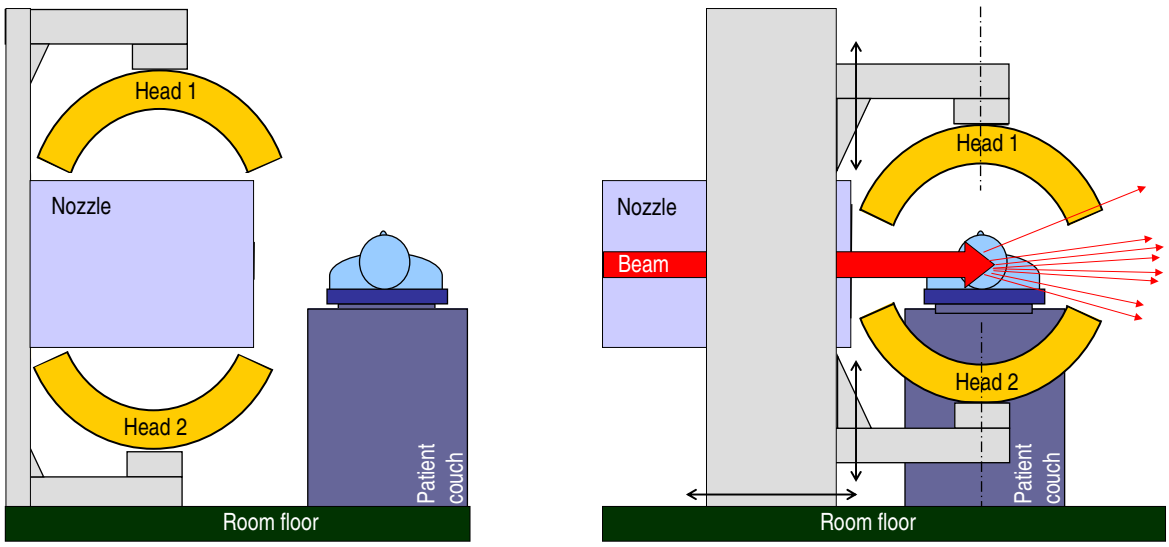

Figure 3.7: Dual-head, small-gaps in-beam PET at a fixed, horizontal beam line. The left image shows the two detector heads in a possible park position, whereas in the right the heads are positioned for data taking during irradiation, with the couch at an angle $\chi = 90°$.

3.7 Summary and Outlook

An isocentric, ion beam delivery (gantry) offering almost no restrictions in beam portal selection, i.e. close to full 3D beam entrance coverage, was previously seen to bring clinical advantages for treating more delicate therapeutic situations [Jäk00]. In order to monitor these precise irradiation fields, in-beam PET with the highest possible image quality is a requisite. In the present chapter three configurations for installing an in-beam positron tomograph onto an isocentric, ion beam delivery were studied. Several technical restrictions arise when addressing the installation issue, and any of them must be respected, namely: (1) fast accessibility of the medical personnel to the patient at all times; (2) collision-free solution concerning in-beam PET, beam nozzle and patient and couch; (3) collision-free solution concerning in-beam PET and the incoming and outgoing particle flux [Gun04a, Gun04b]; (4) volume minimized tomograph due to integration reasons; (5) magnetic field insensitive detectors due to the close proximity, at different distances and changing beam energies, of the last beam bending magnet; and (6) state-of-the-art detectors providing optimum γ-ray detection efficiency as well as energy and time resolutions. Items (4), (5) and (6) are discussed and optimized in the next three chapters.

In order to evaluate the feasibility of three in-beam PET implementation configurations in what regards items (2) and (3) above, a collision table scheme previously defined was used. This scheme shows that an in-beam PET configuration with either a closed-ring or a dual-head tomograph installed at the patient couch results in a forbidden irradiation of a great part of necessary cranio-caudal portals. This is due to the interference of the particle flux leaving the target with the PET support material, which may cause its activation and, therefore, would veto this installation due to radiation protection issues.

A second configuration analyzed consisted in installing a dual-head positron tomograph on a separate gantry, with this gantry being positioned inside the treatment room, opposite to the patient couch [Eng03]. It was seen that this configuration provides a solution regarding items

(2) and (3) during in-beam PET measurements, therefore allowing any portal to be delivered. But it was also seen that, due to the complex PET positioning system, it fails to satisfy requisite (1).

A third configuration, developed at GSI for a dual-head tomograph [Kop04], installs the PET scanner and all its support and driver machinery at the beam nozzle. This solution seems to satisfy all the requisites mentioned. In addition, it was seen that this configuration further allows a closed-ring detector geometry to be implemented, which brings an important enhancement of the quality of in-beam PET images (chapter 2). Nevertheles, there are disadvantages of bringing the PET detectors close to the last beam bending magnet. These are addressed and a solution is proposed in chapter 4. In summary, it seems that the implementation of a closed-ring tomograph fully installed on the beam nozzle brings the best answer for in-beam PET at a rotating, isocentric ion beam delivery.

In what concerns in-beam PET at a fixed, horizontal beam line, a solution complementing that installed at BASTEI elucidates the feasibility of installing both a closed-ring as well as a dual-head, small-gaps positron tomograph at such beam lines.